Journal of Power Sources 196 (2011) 5115–5121

Contents lists available at ScienceDirect

Journal of Power Sources

journal homepage: www.elsevier.com/locate/jpowsour

Modelling the thermal behaviour of a lithium-ion battery during charge

Ui Seong Kim[a], Jaeshin Yi[a], Chee Burm Shin[a,*], Taeyoung Han[b], Seongyong Park[c]

[a] Dept. of Chemical Engineering and Division of Energy Systems Research, Ajou University, 5 Wonchun-Dong, Suwon 443-749, Republic of Korea
[b] Vehicle Development Research Lab., GM R&D Center, MI 48090-9055, USA
[c] Advanced Technology Team, GM Daewoo Auto & Technology, Inchon 403-714, Republic of Korea

ARTICLE INFO

Article history:
Received 10 November 2010
Received in revised form 5 January 2011
Accepted 20 January 2011
Available online 26 February 2011

Keywords:
Lithium-ion battery
Model
Thermal behaviour
Finite element method

ABSTRACT

A method for modelling the thermal behaviour of a lithium-ion battery (LIB) during charge is presented. The effect of charge conditions on the thermal behaviour is examined by means of the finite element method. A comparison of the experimental charge curves with the modelling results validates the two-dimensional modelling of the potential and current density distribution on the electrodes of an LIB as a function of charge time during constant-current charge followed by constant-voltage charge. The heat generation rates as a function of the charge time and the position on the electrodes are calculated to predict the temperature distributions of the LIB based on the modelling results for potential and current density distributions. The temperature distributions obtained from the modelling are in good agreement with the experimental measurements.

1. Introduction

The lithium-ion battery (LIB) is the preferred power source for hybrid electric vehicles (HEVs) and electric vehicles (EVs) due to its high specific energy, high voltage, and low self-discharge rate. To provide affordable HEVs and EVs with satisfactory performance, there are still major technical challenges to improve the characteristics of LIBs such as low cost, high specific energy, high power density, long service life, and proven safety. Because safety is one of the major challenges for the LIB in HEV and EV applications, the thermal control of LIBs is especially important. The main concern in the thermal control of LIB is the significant temperature increase that can occur during high power extraction and rapid charging in HEV and EV applications, which may cause battery degradation and thermal runaway. Thermal modelling can play a key role in controlling the operating temperature and temperature uniformity of LIBs within a suitable range [1–3].

There have been many previous studies of the thermal modelling of LIBs [4–21]. Bernardi et al. [4] developed a general energy balance for battery systems including the contributions from electrochemical reactions, mixing enthalpies and phase changes. Rao and Newman [5] presented a method of calculating the heat generation rate based on the general energy balance and the enthalpy potential method for a LIB system. Chen and Evans [6–8] developed two and three dimensional models to study the thermal behaviour of lithium polymer batteries (LPBs) and LIBs. They assumed that the heat generation rate is uniform throughout the cell. Pals and Newman presented a one-dimensional model for predicting the thermal behaviour of LPBs for a single cell [9] and a cell stack [10]. Verbrugge [11] modelled the three-dimensional current and temperature distributions in LPB modules. Botte et al. [12] studied the influence of design variables on the thermal behaviour of LIBs based on a one-dimensional model. Al-Hallaj et al. [13] presented simplified one-dimensional thermal modelling with lumped parameters to simulate the temperature profiles inside LIB cells. Song and Evans [14] developed an electrochemical–thermal model of LPBs by coupling a two-dimensional thermal model with a one-dimensional electrochemical model. Gu and Wang [15] and Srinivasan and Wang [16] developed a two-dimensional thermal and electrochemical coupled model to analyze the electrochemical and thermal behaviour of lithium-ion battery cells. Gomadam et al. [17] reduced a two-dimensional heat conduction model to a one-dimensional model for LIBs with a spiral geometry by a coordinate transformation approach. Chen et al. [18] developed a three-dimensional model of LIBs considering the location-dependent convection and radiation at the boundaries to reflect the different heat dissipation performances on all of the surfaces. Kim et al. [19,20] presented two-dimensional thermal modelling based on the potential and current density distributions obtained by the same procedure as that described by Kwon et al. [21].

Most of the thermal modelling studies of LIBs and LPBs mentioned above [4–6,9] focused on the thermal behaviour during discharge and only a couple [7,8] briefly dealt with the thermal behaviour during charge to accommodate the dynamic cycling of batteries for EV applications. Although the heat generation rate during charge is less than that during discharge at the same rated

* Corresponding author. Tel.: +82 31 219 2388; fax: +82 31 219 1612.
E-mail address: cbshin@ajou.ac.kr (C.B. Shin).

0378-7753/$ – see front matter © 2011 Elsevier B.V. All rights reserved.
doi:10.1016/j.jpowsour.2011.01.103

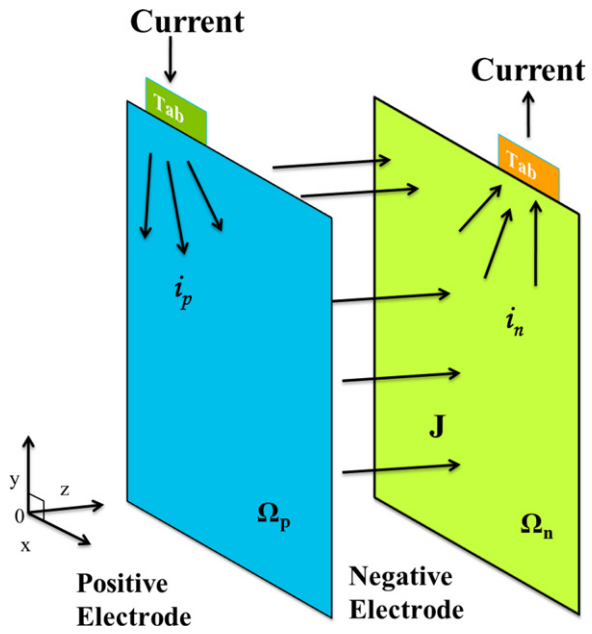

Fig. 1. Schematic diagram of current flow in parallel plate electrodes of a battery.

current of the battery, the increase in local temperature becomes significant during rapid charge especially for the large-size LIBs used in EV and HEV applications [3]. Because there can be many circumstances under which rapid charge becomes a necessity for EV and plug-in HEV applications [22–24], it is important to develop a reliable modelling methodology to predict accurately the thermal behaviour of LIBs under various charge conditions for the purpose of improving their performance and life, as well as ensuring thermal safety. In this work, two-dimensional modelling is performed to calculate the potential and current density distributions during charge on the electrodes of an LIB using a procedure similar to that reported by Kwon et al. [21]. The modelling is validated by comparing the experimental and modelled charge curves at charge rates of 1, 3, and 5 C. Then, the thermal behaviour is modelled as a combination of the heat generation due to the electrochemical reactions and electrical resistance within the cell as a function of the electric current and state-of-charge (SoC) using a similar procedure to that described by Kim et al. [19,20]. The electrical heating rate is calculated from the electrical current flow, which can be evaluated based on the potential distributions on the electrodes obtained from the electrochemical modelling. The thermal model is validated by comparing the modelling results with the experimental measurements.

Table 1
Fitting parameters used to calculate potential and current density distributions on electrodes.

Parameter	Value
a_0 (V)	4.135
a_1 (V)	−0.91
a_2 (V)	1.405
a_3 (V)	−1.48
a_4 (A m^{-2})	116.859
a_5 (A m^{-2})	−892.8001
a_6 (A m^{-2})	5250.46
a_7 (A m^{-2})	−13,623.09
a_8 (A m^{-2})	15,853.17
a_9 (A m^{-2})	−6757.8539

Table 2
Parameters used for thermal modelling.

Component	Density (g cm^{-3})	Heat capacity (J g^{-1} K^{-1})	Thermal conductivity (W cm^{-1} K^{-1})
Current-collector of positive electrode	2.7	0.9	2.38
Electrode material of positive electrode	1.5	0.7	0.05
Current-collector of negative electrode	8.96	0.385	3.98
Electrode material of negative electrode	2.5	0.7	0.05
Separator	1.2	0.7	0.01
Pouch	1.15	1.9	0.16×10^{-2}

2. Mathematical model

A 14.6 Ah LIB comprising a $LiMn_2O_4$ cathode, a graphite anode, and a plasticized electrolyte from LG Chem. was modelled in this work. A cell consisting of two parallel-plate electrodes of the battery shown in Fig. 1 was chosen, because the battery consisted of the same repeating units of positive and negative electrode plates, polymer electrolytes and separators. The tabs are the current-collectors extending outside from the rectangular electrodes and they do not contain the electrode (active) material. A schematic diagram of the current flow in the cell during charge is also included in Fig. 1. The distance between the electrodes was assumed to be so small that the current flow between the electrodes would be perpendicular to them. The modelling procedure used to calculate the potential and current density distribution on the electrodes was similar to that used by Kwon et al. [21]. From the continuity of the current on the electrodes, the following equations could be derived:

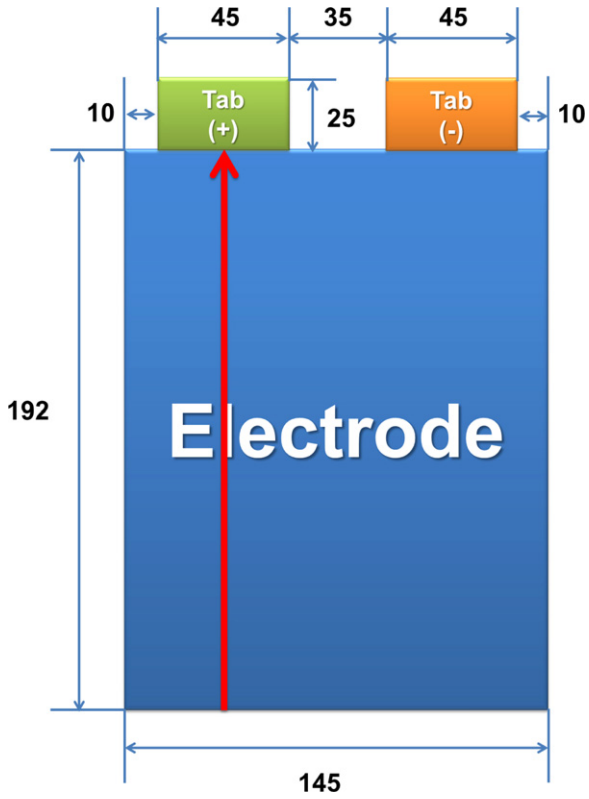

Fig. 2. Dimensions of electrodes and positions of tabs of a 14.6 Ah LIB from LG Chem. Dimensions in mm. Arrow passing through tab from positive electrode represents a vertical line along which temperature distributions are plotted in Fig. 9.

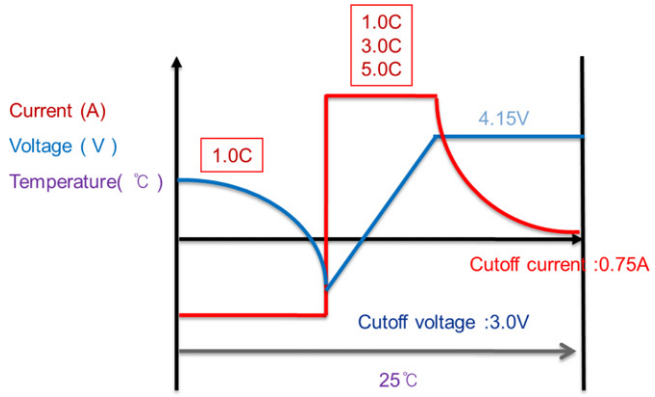

Fig. 3. Schematic illustration of discharge–charge protocol of battery.

$$\nabla \cdot \vec{i}_p + J = 0 \quad \text{in} \quad \Omega_p \tag{1}$$

$$\nabla \cdot \vec{i}_n - J = 0 \quad \text{in} \quad \Omega_n \tag{2}$$

where: $\vec{i}_p$ and $\vec{i}_n$ are the linear current density vectors (current per unit length ($A\,m^{-1}$)) in the positive and negative electrodes, respectively; J is the current density (current per unit area ($A\,m^{-2}$)) transferred through the separator from the negative electrode to the positive electrode; Ω_p and Ω_n denote the domains of the positive and negative electrodes, respectively. According to Ohm's law, $\vec{i}_p$ and $\vec{i}_n$ can be written as:

$$\vec{i}_p = -\frac{1}{r_p}\nabla V_p \quad \text{in} \quad \Omega_p \tag{3}$$

$$\vec{i}_n = -\frac{1}{r_n}\nabla V_n \quad \text{in} \quad \Omega_n \tag{4}$$

where: r_p and r_n are the resistances (Ω) of the positive and negative electrodes, respectively; V_p and V_n are the potentials (V) of the positive and negative electrodes, respectively. The resistances, r_p and r_n, were calculated as described in Refs. [19–21]. The following Poisson equations for V_p and V_n were obtained by substituting Eqs. (3) and (4) into Eqs. (1) and (2), respectively:

$$\nabla^2 V_p = +r_p J \quad \text{in} \quad \Omega_p \tag{5}$$

$$\nabla^2 V_n = -r_n J \quad \text{in} \quad \Omega_n \tag{6}$$

The relevant boundary conditions for V_p were:

$$\frac{\partial V_p}{\partial n} = 0 \quad \text{on} \quad \Gamma_{p_1} \tag{7}$$

$$\frac{1}{r_p}\frac{\partial V_p}{\partial n} = \frac{I_0}{L} \quad \text{on} \quad \Gamma_{p_2} \tag{8}$$

where: $\partial/\partial n$ denotes the gradient in the direction of the outward normal to the boundary. The first boundary condition (7) implies that there is no current flow through the boundary (Γ_{p1}) of the electrode other than the tab. The second boundary condition (8) means that the linear current density through the tab (Γ_{p2}) of length L (cm) is constant with a value of I_0/L, where I_0 is the total current (A) through the tab in the mode of constant-current charge, for which the boundary condition at Γ_{p2} becomes simply $V_p = V_c$ where V_c is the fixed value of charge voltage. The boundary conditions for V_n are:

$$\frac{\partial V_n}{\partial n} = 0 \quad \text{on} \quad \Gamma_{n_1} \tag{9}$$

$$V_n = 0 \quad \text{on} \quad \Gamma_{n_2} \tag{10}$$

The first boundary condition (9) implies the same as in the case of V_p. The second boundary condition (10) means that the potential at the tab of the negative electrode has a fixed value of zero as the reference potential. The difference between the governing equations for charge used in this work and those for discharge is that the signs in front of J in Eqs. (1), (2), (5) and (6) are opposite to those in the corresponding equations of the previous studies [19–21]. The only difference between the boundary conditions for charge used in this work and those for discharge is that the sign in front of I_0 in Eq. (8) is opposite to that in the corresponding boundary condition of the previous investigations [19–21].

The current density, J, of Eqs. (5) and (6) is a function of the potential difference between the positive and the negative electrodes ($V_p - V_n$). The functional form depends on the polarization characteristics of the electrodes. In this work, the following polarization expression used by Tiedemann and Newman [25] and Newman and Tiedemann [26] was adopted

$$J = Y(V_p - V_n - U) \tag{11}$$

where Y and U are the fitting parameters. As suggested by Gu [27], U and Y were expressed as functions of the depth-of-discharge (DoD) as follows:

$$U = a_0 + a_1(\text{DoD}) + a_2(\text{DoD})^2 + a_3(\text{DoD})^3 \tag{12}$$

$$Y = a_4 + a_5(\text{DoD}) + a_6(\text{DoD})^2 + a_7(\text{DoD})^3 + a_8(\text{DoD})^4 + a_9(\text{DoD})^5 \tag{13}$$

where a_0–a_9 are constants to be determined experimentally. The fitting parameters used to calculate the potential and current density distribution on the electrodes are listed in Table 1.

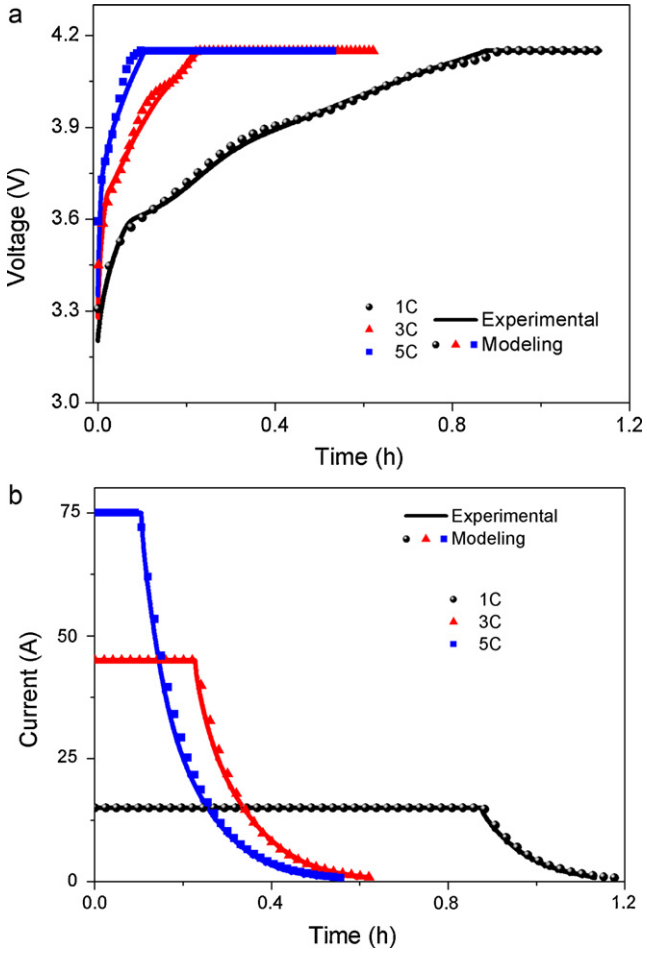

Fig. 4. Variations of (a) charge voltage and (b) charge current during CC–CV charging.

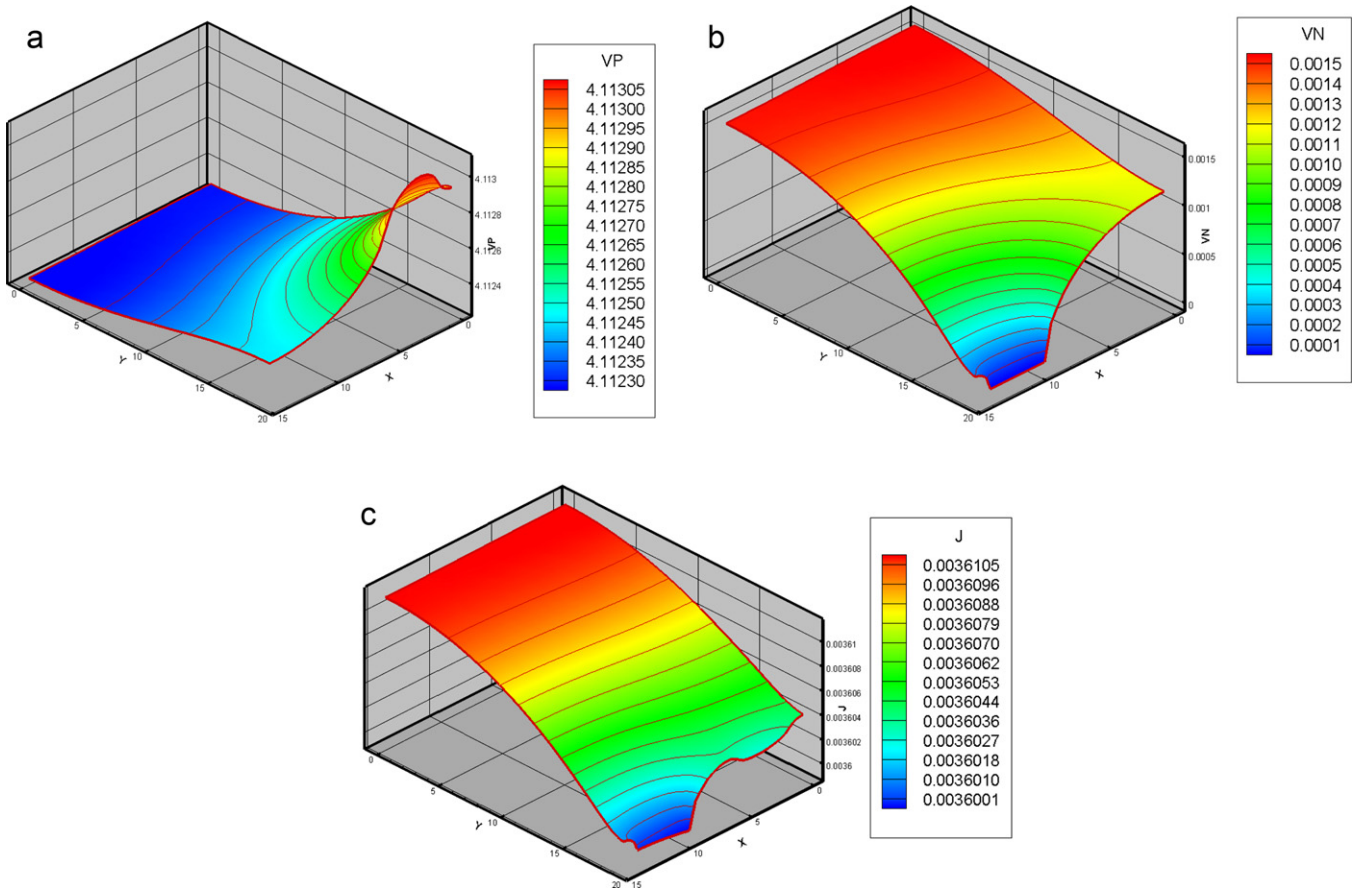

Fig. 5. Distributions of (a) potential on positive electrode, (b) potential on negative electrode and (c) current density on electrodes of LIB at charge time of 45 min during CC charging at 1 C.

By solving the equations listed previously, the distribution of the current density, J, on the electrodes can be obtained as a function of the position on the electrode and time. Therefore, the DoD varies with the position on the electrode and the time elapsed during charge. The distribution of DoD on the electrode could be calculated from the distribution of J as follows:

$$\mathrm{DoD} = \mathrm{DoD}_0 - \frac{\int_0^t J\ \mathrm{d}t}{Q_T} \tag{14}$$

where: DoD_0 is the initial value of DoD; t is the charge time (s); Q_T is the theoretical capacity per unit area ($\mathrm{Ah\,m^{-2}}$) of the electrodes.

The thermal modelling procedure was used to calculate the temperature distribution on the electrodes was similar to that used by Kim et al. [19,20]. Since the thickness of the battery cell was much shorter than its other dimensions, the temperature variation along the z direction in Fig. 1 could be neglected. Based on the differential energy conservation for a battery, the transient two-dimensional equation of heat conduction was written as follows:

$$\rho C_p \frac{\partial T}{\partial t} = \frac{\partial}{\partial x}\left(k_x \frac{\partial T}{\partial x}\right) + \frac{\partial}{\partial x}\left(k_y \frac{\partial T}{\partial y}\right) + q - q_{conv} \tag{15}$$

where: ρ is the density ($\mathrm{kg\,m^{-3}}$); C_p is the volume averaged specific heat capacity at constant pressure ($\mathrm{J\,kg^{-1}\,{}^\circ C^{-1}}$); T is the temperature (°C); k_x and k_y are the effective thermal conductivities along the x and y directions (refer to Fig. 1 for the x and y directions) ($\mathrm{W\,m^{-1}\,{}^\circ C^{-1}}$), respectively, q is the heat generation rate per unit volume ($\mathrm{W\,m^{-3}}$); q_{conv} is the heat dissipation rate ($\mathrm{W\,m^{-3}}$) through the surfaces of the battery by convection. The effective thermal conductivities of the various compartments of the cell could be estimated based on the equivalent networks of parallel and series thermal resistances of the cell components [7,18].

The heat generation rate, q, was given as follows:

$$q = aJ\left[E_{oc} - E - T\frac{dE_{oc}}{dT}\right] + a_p r_p i_p^2 + a_n r_n i_n^2 \tag{16}$$

where: a is the specific area of the battery ($\mathrm{m^{-1}}$); J is the current density ($\mathrm{A\,m^{-2}}$) calculated by Eq. (8); E_{oc} is the open-circuit potential of the cell (V), E is the cell voltage (V), a_p and a_n are the specific area of the positive and negative electrodes ($\mathrm{m^{-1}}$), respectively; i_p and i_n are the magnitudes of the vectors $\vec{i}_p$ and $\vec{i}_n$ obtained by Eqs. (3) and (4) ($\mathrm{A\,m^{-1}}$), respectively. The detailed definition of each term on the right-hand side of Eq. (16) was described in Refs. [16,19,28]. The heat dissipation rate, q_{conv}, was derived as follows:

$$q_{conv} = \frac{2h}{d}(T - T_{air}) \tag{17}$$

where: h is the convective heat-transfer coefficient on the surfaces of the battery ($\mathrm{W\,m^{-2}\,{}^\circ C^{-1}}$); d is the thickness of the battery cell in the direction perpendicular to the parallel electrodes (m); T_{air} is the ambient temperature (°C). The rate was rendered by approximating a three-dimensional object to a two-dimensional one, as shown in Eq. (15). The convective boundary condition applied to the boundaries of the electrode is reported by Kim et al. [19]. The parameters used for the thermal modelling are listed in Table 2.

3. Results and discussion

The solutions to the governing Eqs. (5), (6) and (15) subject to the associated boundary conditions were obtained using the finite

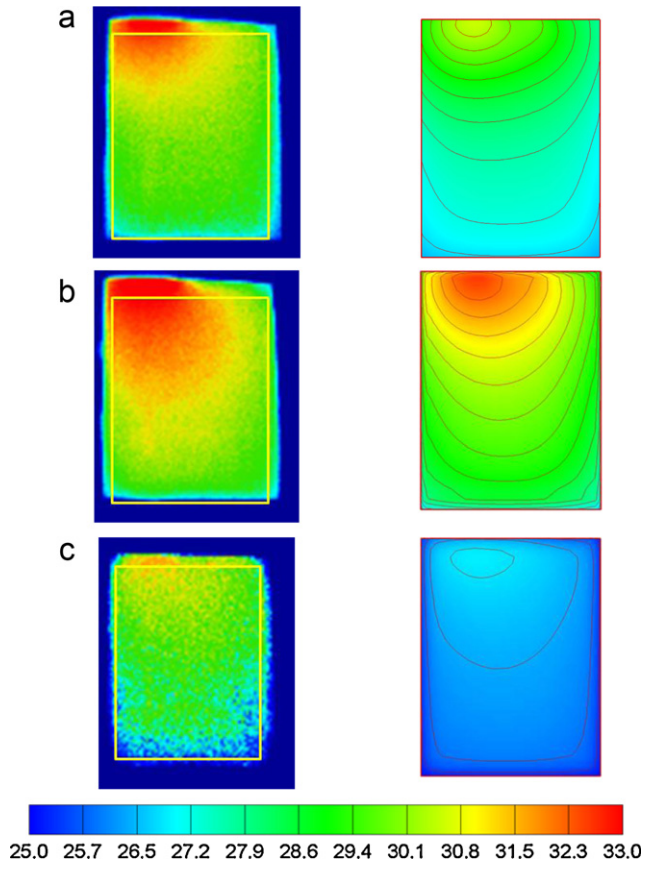

Fig. 6. Temperature distributions based on experimental IR image and modelling for LIB at charge times of (a) 8 min, (b) 16 min and (c) 36 min during CC–CV charging with CC charge at 3 C.

element method. The finite element package used is an in-house code specifically developed to solve the problem defined in this work. In order to test the validity of the model, experiments were carried out at a room temperature of 25 °C using a 14.6 Ah LIB fabricated by LG Chem, of which the dimensions of the electrodes and the positions of the tabs are shown in Fig. 2. The experimental procedures are illustrated schematically in Fig. 3. To maintain the same states-of-charge before the beginning of the charge experiments, the battery was discharged under the constant-current (CC) rate of 1 C until the voltage dropped to the cut-off voltage of 3.0 V and then it was allowed to rest for 8 h. The battery was charged with CC rates of 1, 3, and 5 C until the voltage reached the predetermined value of 4.15 V. Then, the charging voltage was kept constant at 4.15 V until the charge current tapered to 0.75A and this charging mode is referred to herein as constant-voltage (CV) charging.

The variation of the voltage and current of the battery during CC–CV charging, is shown, in Fig. 4(a) and (b). The modelling results and experimental measurements are in good agreement with each other. The model predicts a decrease in the CC charging time and an increase in the CV charging time with increasing rates of CC charging. The distributions of potential and current density on the electrodes during charge were obtained as a function of time for various charge rates. As an example, Fig. 5(a)–(c) shows the distributions of the potential on the positive electrode, the potential on the negative electrode, and the current density at a charge time of 45 min during CC charging at 1 C, respectively. In Fig. 5(a), the potential gradient on the positive electrode appears to be most severe in the region where the tab is attached to the current-collector. This is because all of the current flows through the conducting current collector from the tab into the entire electrode plate. Again, the potential gradient on the negative electrode shown in Fig. 5(b) is the highest in the region near the tab, because all of the current needs to flow from the entire electrode plate into the tab. The non-uniform distributions of current density transferred from the positive electrode to the negative electrode during CC charging at 1 C are presented in Fig. 5(c).

After obtaining the distributions of potential and current density on the electrodes during charge, the temperature distributions of the battery can be calculated as a function of time for various charge rates using Eq. (15). As a demonstration, Fig. 6(a)–(c) shows the temperature distributions based on the experimental IR image and the modelling for a 14.6 Ah LIB at charge times of 8, 16 and 36 min during CC–CV charging, where the rate of CC charging is 3 C. Similar plots to Fig. 6(a)–(c) are made in Fig. 7(a)–(c) for charge times of 3, 6 and 24 min, respectively, during CC–CV charging, where the rate of CC charging is 5 C. In the IR images, the region within the yellow lines of the rectangle corresponds to the computational domain for the modelling. Therefore, the maximum temperature within the computational domain should be differentiated from that of the current collecting tab protruding beyond the electrode region of the battery cell. The overall temperature distributions obtained from the experiment and model in Figs. 6 and 7, respectively, are in good agreement with each other. The temperature near the current-collecting tab of the positive electrode is higher than that of the negative electrode. This is attributed to the electrical conductivity of the active material of the positive electrode being much lower than that of the negative electrode, even though the current flows near the tabs of both the positive and the negative electrodes are similarly high. The maxi-

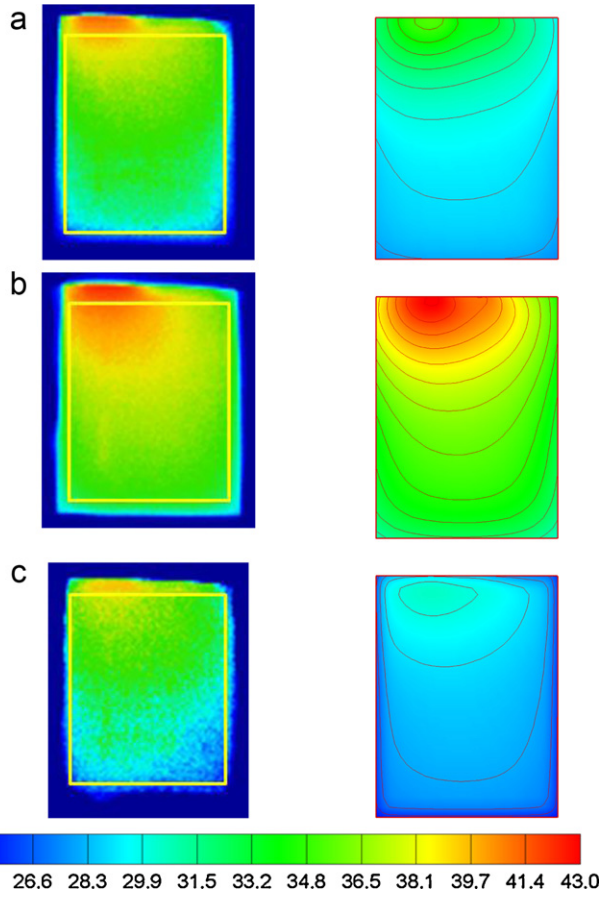

Fig. 7. Temperature distributions based on experimental IR image and modelling for LIB at charge times of (a) 3 min, (b) 6 min and (c) 24 min during CC–CV charging with CC charge at 5 C.

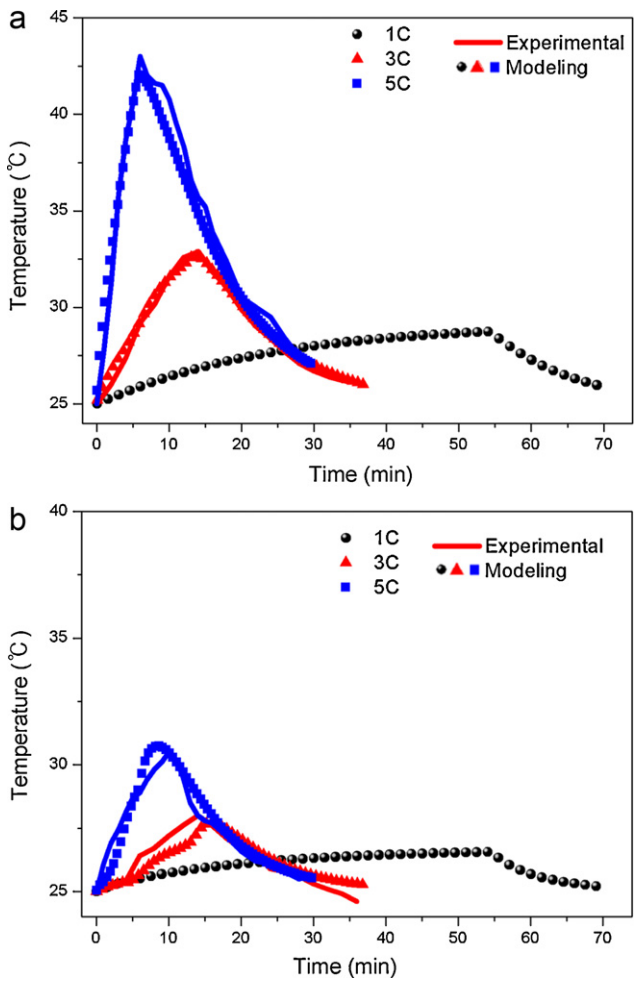

Fig. 8. Comparison of (a) maximum temperatures and (b) minimum temperatures obtained from experiment and model for LIB during CC–CV charging with CC charge at 3 and 5 C. Only modelling results shown for CC charge at 1 C.

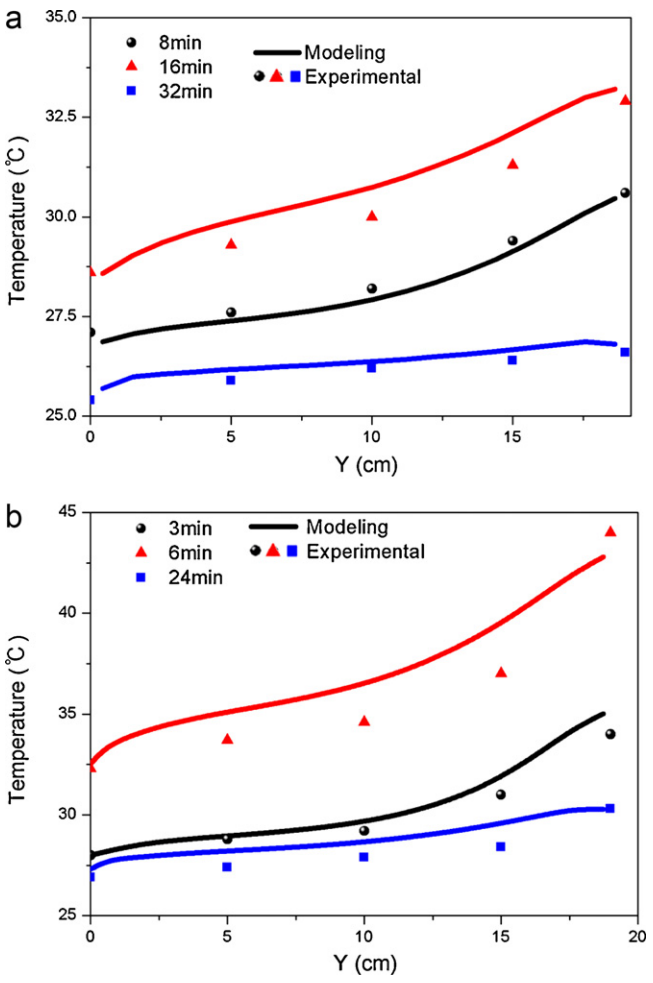

Fig. 9. Comparison of temperature distributions obtained from experiment along vertical line passing through middle of current-collecting tab from positive electrode represented by arrow in Fig. 2 with those obtained from model during CC–CV charging with CC at (a) 3 C and (b) 5 C.

mum and minimum temperatures obtained from the experimental measurements and those predicted by the model, are shown in Fig. 8(a) and (b) respectively. The maximum and minimum temperatures increase during CC charging and then decrease during CV charging, because the heat generation rates decrease rapidly due to the rapid decrease of the charge current during CV charging. The maximum and minimum temperatures obtained from the experiment and modelling are in good agreement with each other over the whole range of DoDs at charge rates of 3 C and 5 C during CC charging. It is not easy, however, to resolve experimentally the increasing and decreasing patterns of the maximum and minimum temperatures during CC–CV charging, when the rate of CC charging is 1 C, because the temperature rise of the battery cell compared with the atmospheric temperature is not as clear as those of CC charging observed at rates of 3 and 5 C. Therefore, only the maximum and minimum temperatures predicted by the model are shown in Fig. 8(a) and (b) in the case of CC charging at 1 C. To compare the details of the temperature distributions obtained from experiment and model quantitatively, the temperature distributions obtained by experiment along a vertical line passing through the middle of the current-collecting tab from the positive electrode, which is represented by a red arrow in Fig. 2, are compared with those obtained from the model in Fig. 9, because the temperature gradient along that line is expected to be higher than that in the other region of the battery. In the case of CC charging at 3 and 5 C, the temperature distributions obtained by experiment are in good agreement with those obtained from the model, although the later are relatively higher than those obtained by experimental when near the end of CC charging. These results suggest that the modelling presented in this study is useful to predict accurately the thermal behaviour during charge for the large-size LIBs used in EV and HEV applications. The modelling can be used to calculate the uneven distribution of heat generation rate in battery cell in order to optimize the cooling strategy of battery packs where rapid charging is needed. The charge model presented in this article can be combined with the discharge model previously reported [19–21] to predict transient behaviour such as the discharge/charge voltage, current, state of charge and uneven temperature distribution of LIB in real-life driving cycles for EV and HEV applications instead of constant-current discharge/charge conditions.

4. Conclusions

A mathematical procedure is developed to study the thermal behaviour of an LIB during charge. The two-dimensional potential and current density distribution on the electrodes of an LIB are predicted as a function of the charge time during CC–CV charging using the finite element method. By comparing the experimental charge curves with the modelling results during CC–CV charging with CC charge rates of 1, 3, and 5 C, the modelling of the potential and current density distributions on the electrodes is validated.

Then, based on the results of modelling of the potential and current density distributions, the heat generation rate as a function of the charge time and the position on the electrodes is calculated to predict the thermal behaviour of the LIB. The two-dimensional temperature distributions obtained from the experiment and modelling are in good agreement with each other during the whole process of CC–CV charging. The modelling methodology presented in this study may contribute to optimization of the cooling strategy of battery packs to improve the performance and life of LIBs, as well as to ensuring their thermal safety in applications where rapid charging is required.

Acknowledgements

The work was supported by General Motors Corporation. One of the authors (C.B. Shin) acknowledges the National Research Foundation of Korea (NRF 2009-0064626 and NRF 2010-0025353) and the Ministry of Commerce, Industry and Energy of Republic of Korea (2007-E-1D25-P-02-0-00) for partial financial support.

References

[1] G. Ceder, M. Doyle, P. Arora, Y. Fuentes, MRS Bull. 27 (2002) 619–623.
[2] J. Newman, K.E. Thomas, H. Hafezi, D.R. Wheeler, J. Power Sources 119–121 (2003) 838–843.
[3] R. Spotnitz, J. Franklin, J. Power Sources 113 (2003) 81–100.
[4] D. Bernardi, E. Pawlikowski, J. Newman, J. Electrochem. Soc. 132 (1985) 5–12.
[5] L. Rao, J. Newman, J. Electrochem. Soc. 144 (1997) 2697–2704.
[6] Y. Chen, J.W. Evans, J. Electrochem. Soc. 140 (1993) 1833–1838.
[7] Y. Chen, J.W. Evans, J. Electrochem. Soc. 141 (1994) 2947–2955.
[8] Y. Chen, J.W. Evans, J. Electrochem. Soc. 143 (1996) 2708–2712.
[9] C.R. Pals, J. Newman, J. Electrochem. Soc. 142 (1995) 3274–3281.
[10] C.R. Pals, J. Newman, J. Electrochem. Soc. 142 (1995) 3282–3288.
[11] M.W. Verbrugge, AIChE J. 41 (1995) 1550–1562.
[12] G.G. Botte, B.A. Johnson, R.E. White, J. Electrochem. Soc. 146 (1999) 914–923.
[13] S. Al-Hallaj, H. Maleki, J.S. Hong, J.R. Selman, J. Power Sources 83 (1999) 1–8.
[14] L. Song, J.W. Evans, J. Electrochem. Soc. 147 (2000) 2086–2095.
[15] W.B. Gu, C.Y. Wang, in: S. Surampudi, R.A. Marsh, Z. Ogumi, J. Prakashi (Eds.), Lithium Batteries, The Electrochemical Society, Pennington, NJ, 2000, pp. 748–763.
[16] V. Srinivasan, C.Y. Wang, J. Electrochem. Soc. 150 (2003) A98–A106.
[17] P.M. Gomadam, R.E. White, J.W. Weidner, J. Electrochem. Soc. 150 (2003) A1339–A1345.
[18] S.C. Chen, C.C. Wan, Y.Y. Wang, J. Power Sources 140 (2005) 111–124.
[19] U.S. Kim, C.B. Shin, C.-S. Kim, J. Power Sources 180 (2008) 909–916.
[20] U.S. Kim, C.B. Shin, C.-S. Kim, J. Power Sources 189 (2009) 841–846.
[21] K.H. Kwon, C.B. Shin, T.H. Kang, C.-S. Kim, J. Power Sources 163 (2006) 151–157.
[22] B. Kang, G. Ceder, Nature 458 (2009) 190–193.
[23] M. Okubo, E. Hosono, J. Kim, M. Enomoto, N. Kojima, T. Kudo, H. Zhou, I. Honma, J. Am. Chem. Soc. 129 (2007) 7444–7452.
[24] C.-K. Park, Z. Zhang, Z. Xu, A. Kakirde, K. Kang, C. Chai, G. Au, L. Cristo, J. Power Sources 165 (2007) 892–896.
[25] W. Tiedemann, J. Newman, in: S. Gross (Ed.), Battery Design and Optimization, The Electrochemical Society, Princeton, NJ, 1979, pp. 39–49.
[26] J. Newman, W. Tiedemann, J. Electrochem. Soc. 140 (1993) 1961–1968.
[27] H. Gu, J. Electrochem. Soc. 130 (1983) 1459–1464.
[28] C.Y. Wang, V. Srinivasan, J. Power Sources 110 (2002) 364–376.